Break it down to speed it up: Na₂O–NaTaCl₆

Islamiyat A. Ojelade,†[ab] Erica Truong,†[ab] Ifeoluwa P. Oyekunle,[ab] Tej P. Poudel,[c] Yudan Chen,[ab] Michael J. Deck,[ab] Yongkang Jin,[ab] Bright Ogbolu,[ab] Pawan K. Ojha, [ab] Md. Mahinur Islam,[ab] Thilina N. D. D. Gamaralalage,[ab] J. S. Raaj Vellore Winfred[a] and Yan-Yan Hu [*abc]

Fast sodium-ion conductors hold strong potential for enabling all-solid-state sodium batteries, offering inherent advantages such as enhanced safety and cost-effectiveness. However, challenges remain in achieving fast ion transport for realizing high-power density. This work reports the synthesis of a novel sodium solid electrolyte, Na₂O–NaTaCl₆ (Na₂O-NTC), *via* an energy-efficient approach. We achieved a high ionic conductivity of 4.41 mS cm⁻¹ and activation energy of 0.32 eV with only 4 hours of mechanochemical milling. The conductivity of Na₂O-NTC surpassed that of crystalline NaTaCl₆ (NTC) synthesized under similar conditions by more than one order of magnitude. In addition, Na₂O-NTC exhibited a relatively low electronic conductivity of 6.72×10^{-10} S cm⁻¹. Using XRD, Raman, and high-resolution NMR characterizations, the presence of Na₂O as a glass modifier was found to effectively amorphize the crystalline structure of NaTaCl₆, resulting in a glassy oxyhalide material with fast Na⁺ dynamics. This work demonstrates that leveraging inexpensive glass modifiers can effectively break down low-conductivity crystalline materials and tune the local structures to obtain highly conductive glassy solid electrolytes. Cost-effective and energy-efficient synthesis of glassy superionic conductors can aid the development and widespread adoption of high-performance rechargeable solid-state Na batteries.

Introduction

The increasing demand for energy necessitates the use of renewable energy sources, accompanied by advanced energy storage technologies. All-solid-state batteries (ASSBs) are considered the next-generation energy storage technology, as they offer a potential solution to the safety concerns and energy density limits associated with the current liquid-electrolyte-based batteries.[1–8] Although Li-ion batteries have dominated the electrochemical energy storage research space, Na-ion batteries are also gaining attention as a viable alternative to lithium-ion batteries, primarily because of the high natural abundance and low cost of Na, thus making Na-ion batteries a more sustainable option for large-scale energy storage. However, developing sodium solid electrolytes (Na-SE) with high ionic conductivity and good stability to enable high-power-density batteries remains challenging.[3,7,9–11]

Considerable efforts have been made to develop Na-SE, focusing on three main categories of inorganic solid electrolytes: oxides, sulfides, and halides. Oxides such as the NASICON structures $(Na_{3+x}M_yM'_{2-y}S_{2-z}P_z O_{12} M = Ca, Mg, Zn, Ti, N, La)$ are well-known for their high chemical and electrochemical stability; however, achieving high ionic conductivity for oxides often requires high-temperature sintering.[12–15] Sulfides and their derivatives (Na_3PS_4, $Na_{3.0}PS_{3.8}Cl_{0.2}$, $Na_3PS_{4-x}O_x$) are soft and exhibit high ionic conductivity, but their poor chemical and electrochemical stability hinders their practical application in ASSBs.[16–20] Halide-based Na-SEs, including Na_2ZrCl_6 (NZC), Na_2YCl_6 (NYC), $Na_{3-x}Y_{1-x}Zr_xCl_6$ (NYZC), and Na_2TaCl_6 (NTC), are attractive owing to their promising ionic conductivity and electrochemical stability at high voltages.[21–28]

Structurally, these inorganic solid electrolytes can exist in either crystalline or amorphous forms. Crystalline SEs have well-defined, long-range structures, which provide predictable pathways for ion transport. However, ion transport is often slowed down due to the presence of grain boundaries and bottlenecks along the diffusion channels.[7,29–31] Additionally, grain boundaries cause dendrite formation and short circuiting of batteries.[32] In contrast, the lack of grain boundaries in glassy materials minimizes dendrite formation and potentially elongates battery lifetime. Glassy SEs lack structural periodicity, and thus, they do not have well-defined ion transport pathways like

aDepartment of Chemistry and Biochemistry, Florida State University, Tallahassee, FL 32306, USA. E-mail: yhu@fsu.edu

bCenter of Interdisciplinary Magnetic Resonance, National High Magnetic Field Laboratory, Tallahassee, FL 32310, USA

cMaterials Science and Engineering Program, Florida State University, Tallahassee, FL 32306, USA

† These authors contributed equally.

in crystalline SEs. Therefore, glassy materials often exhibit poorer ionic conductivities. Since ion transport in glassy SEs highly depends on local structures and lattice dynamics, the creation of a more flexible local network can be conducive to fast ion movement, potentially leading to higher ionic conductivity.[8,33–37] Glass modifiers such as Na_2O, Li_2O, and Ag_2O play crucial roles in effectively modifying the anion network and creating bridging and non-bridging oxygen atoms within the glass network, thereby facilitating the formation of favorable conduction pathways for ion movement.[14,38–40] Consequently, glassy Na-SEs with enhanced performance can be developed by introducing glass modifiers into their crystalline structures, creating structural disorder and diffusion pathways for fast Na-ion conduction.

Currently, most Na-based glassy SEs that have been developed either require a long synthesis time >40 hours or elevated synthesis temperature; however, the ionic conductivity is still low (<1 mS cm^{-1}) for practical use.[13,31,41–44] Developing high-performance solid electrolytes through energy- and time-efficient methods is paramount for the commercialization of ASSBs. Efficient synthesis methods reduce production costs and time, making the technology more viable for widespread adoption to meet the ever-increasing energy demand. Therefore, developing materials with high performance using energy-efficient methods is crucial for the future of energy storage technologies.

Leveraging glass modifiers, we have synthesized a highly conductive, glassy Na-SE, Na_2O–$NaTaCl_6$ (Na_2O-NTC) via efficient room-temperature mechanochemical synthesis. By mechanochemical ball-milling of the starting materials for just 1, 2, 4, and 6 hours, we achieved ionic conductivity exceeding 1 mS cm^{-1}. The most optimal condition was at 4 hours, producing a remarkable conductivity of 4.41 mS cm^{-1}— over one order of magnitude higher than NTC ball-milled for the same duration. In the glassy Na_2O-NTC, the presence of the glass modifier, Na_2O, disrupted the NTC crystal planes, promoting local ion dynamics and efficient Na-ion conduction. Powder-XRD analysis confirmed the progressive amorphization of the SE with extended milling time. The local structure of the glassy Na_2O-NTC was further elucidated via ^{23}Na magic-angle-spinning (MAS) NMR and Raman spectroscopy, and Na$^+$-ion dynamics probed by NMR relaxometry. This work highlights the potential of inexpensive glass modifiers to promote energy-efficient synthesis of highly conductive Na-based SE.

Experimental methods

Synthesis of Na_2O-NTC

The mechanochemical method was utilized to synthesize Na_2O-NTC. First, Na_2O (Sigma Aldrich, 99.8%) and NaCl (VWR Chemicals BDH) were pre-dried under vacuum at 200 °C for 12 hours, while other materials were used as purchased. In an Argon-filled glovebox (VTI), all the starting materials, Na_2O (Sigma Aldrich, 99.8%), NaCl (VWR Chemicals BDH), and $TaCl_5$ (Sigma Aldrich, 99.8%), were ground in an agate mortar and pestle for 5 minutes using a 1 : 1 molar ratio of Na_2O to $NaTaCl_6$, to form a homogenized mixture. The resulting powder was then

transferred into a 25 mL Zirconia jar containing two 10 mm zirconia balls. The jar was vacuum-sealed to retain the powder in an inert atmosphere and mechanochemically ball-milled for 1, 2, 4, and 6 hours using a high-energy ball mill (SPEX8000M). The synthesized samples were then collected for characterization and stored in an Argon-filled glovebox.

Electrochemical impedance spectroscopy (EIS)

The ionic conductivities of all Na_2O-NTC samples were evaluated using Gamry 600+ over a frequency range of 0.1 Hz to 5 MHz. The powder was pressed at 360 MPa between two steels in house-made 8 mm cylindrical split cells with indium foil as the blocking electrode. To determine the activation energy for ion conduction, variable-temperature EIS (VT-EIS) was performed in a Cincinnati Sub-Zero (CZS) Microclimate Chamber under dry air, within a temperature range of −15 and 55 °C at 10 °C intervals.

DC polarization

DC polarization technique was utilized to determine the electronic conductivities of the synthesized electrolytes. Approximately 130 mg of the solid electrolyte was weighed and pressed between two stainless steels of a 8 mm cylindrical split cell made in-house. Electronic conductivity was measured using Gamry 600+ at 0.1 V. The stainless steel served as the current collector and ion-blocking electrodes.

Materials characterization

Powder X-ray diffraction (P-XRD). The powder X-ray diffraction of NTC and Na_2O-NTC composites was carried out on a Rigaku D8 powder diffractometer. Diffraction patterns were collected using a voltage of 45 kV and current of 40 mA with Cu-Kα radiation over the 2θ range of 10–80° with a step size of 0.03° and at a scan rate of 2.5° per min. To prevent the exposure of Na_2O-NTC samples to humid air, all samples were prepared in an Ar-filled glovebox and protected with a Kapton film. Rietveld refinement was conducted using the GSAS software suite.[45]

Solid-state nuclear magnetic resonance (SS-NMR). Using a Bruker 2.5 mm Magic Angle Spinning (MAS) NMR probe, ^{23}Na MAS NMR experiments were performed on a Bruker NMR spectrometer (500 MHz 11.7 T) at a Larmor frequency of 132.294 MHz. To prepare the sample for the experiment, a 2.5 mm zirconia rotor was packed with approximately 30 mg of sample. ^{23}Na NMR spectra were acquired using a single pulse with a p/2 pulse length of 3.85 μs and a recycle delay of 10 s at a spinning rate of 25 kHz. In addition, ^{23}Na spin-lattice relaxation time (T_1) measurements were measured using an inversion recovery pulse sequence.

Variable-temperature ^{23}Na spin-lattice relaxation time (T_1) measurements were carried out using an inversion recovery pulse sequence on a Bruker Avance-I NMR spectrometer (300 MHz, 7.05 T) at a Larmor frequency of 73.39 MHz, and a spinning rate of 10 kHz. Samples were packed into a 4 mm zirconia rotor. Measurements were performed from 25 to 85 °C with an

increment of 5 °C. ^{23}Na shift was calibrated using 0.1 M NaCl solution at 0 ppm.

Scanning electron microscopy - energy dispersive X-ray spectroscopy (SEM-EDS). Scanning Electron Microscopy (SEM) and Energy Dispersive X-ray Spectroscopy (EDS) were used to examine the morphology and elemental composition of Na$_2$O-NTC. Approximately 130 mg of the synthesized Na$_2$O-NTC powder was pressed into a pellet at 360 MPa, and the analysis was performed using a JEOL JSM-IT800 SEM-EDS system. Images were collected at an accelerating voltage of 15.0 kV with a dwell time of 5 μs.

Raman spectroscopy. Raman spectroscopy was carried out using HORIBA JY LabRam Evolution Raman Spectrograph with a 532 nm excitation laser and a grating size of 600 g mm^{-1}. The powdered samples were placed on glass slides and covered with glass for the analysis.

Results and discussion

Ionic and electronic conductivities

AC electrochemical impedance spectroscopy (EIS) was utilized to determine the conductivities of Na$_2$O-NTC synthesized *via*

mechanochemical milling, as described in the Method section. Fig. 1a shows the room-temperature Nyquist plot of NTC and Na$_2$O-NTC mechanochemically ball-milled for 4 hours, denoted as NTC-4 and Na$_2$O-NTC-4, respectively. The equivalent circuit model for analyzing the Nyquist plots of Na$_2$O-NTC acquired at −25 °C and 25 °C is shown in Fig. S1. From the Nyquist plot analysis, an overall conductivity of 4.41 mS cm^{-1} was obtained for Na$_2$O-NTC-4 , which surpasses that of NTC-4 (0.11 mS cm^{-1}) by over forty times. Only one semicircle in the high-frequency region of the Nyquist plot acquired at −25 °C for Na$_2$O-NTC-4 (Fig. 1b) suggests that bulk and grain boundary contributions to ion transport cannot be resolved, or the grain boundary contribution is negligible in this material.[4,46–48] Variable-temperature electrochemical impedance spectroscopy (VT-EIS) was used to determine the activation energy for Na-ion transport. Fig. 1c shows the Arrhenius-type plot of Na$_2$O-NTC composites synthesized at different ball-milling durations (1, 2, 4, and 6 hours). All Na$_2$O-NTC samples exhibit high ionic conductivities exceeding 1 mS cm^{-1} (Fig. S2, S3a, and Table S1). The activation energy for Na-ion transport ranges from 0.32 eV (Na$_2$O-NTC-4 hours) to 0.36 eV (Na$_2$O-NTC-1 hour). Overall, the activation energy is relatively low compared to other Na-ion
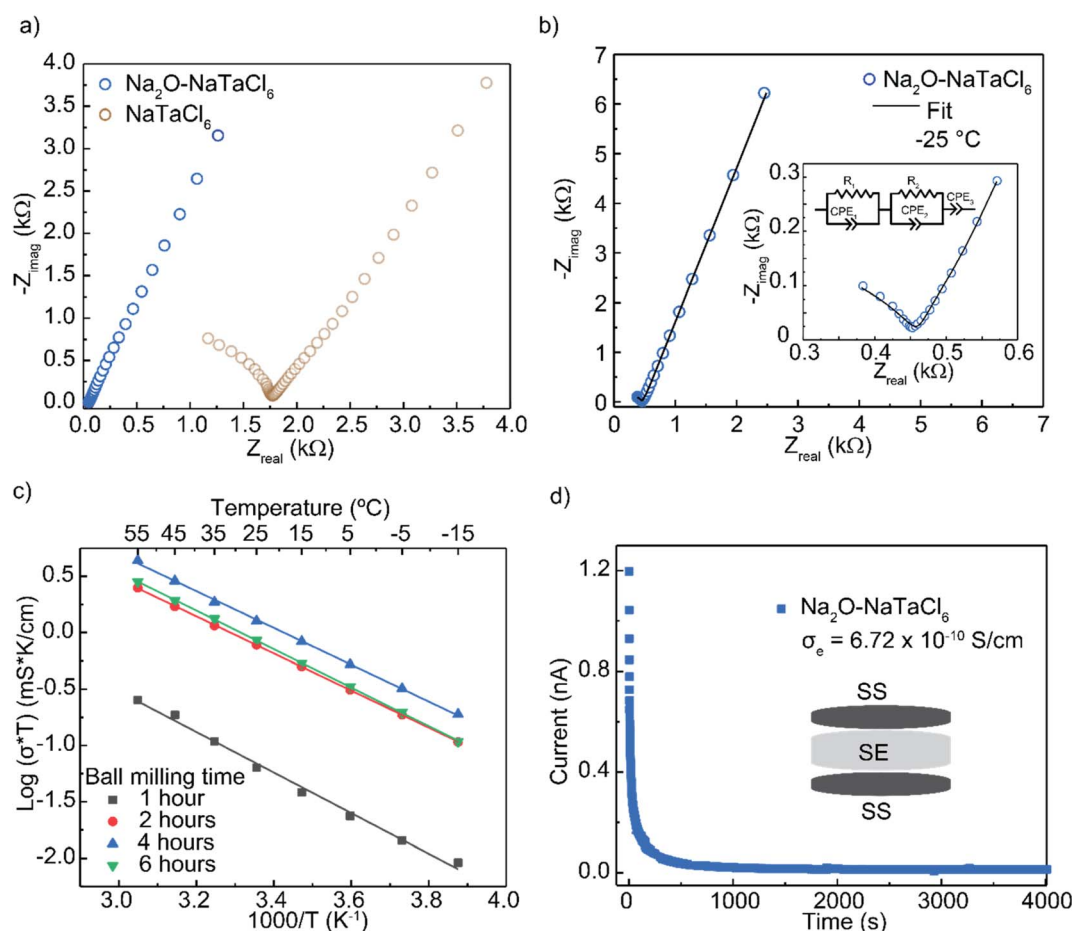
Fig. 1 (a) Nyquist plots of Na$_2$O−NaTaCl$_6$ and NaTaCl$_6$ prepared *via* mechanochemical ball-milling for 4 hours, measured at 25 °C. (b) Nyquist plots for Na$_2$O−NaTaCl$_6$ measured at −25 °C with equivalent circuit fitting (inset). (c) Arrhenius plot of Na$_2$O−NaTaCl$_6$ synthesized *via* mechanochemical ball-milling for 1, 2, 4, and 6 hours. (d) DC polarization curve of Na$_2$O−NaTaCl$_6$ ball-milled for 4 hours and its corresponding electronic conductivity of 6.72 × 10^{-10} S cm^{-1}.

conductors.[24–26] The electronic conductivity of Na_2O-NTC-4 hours was calculated to be 6.72×10^{-10} S cm^{-1} (Fig. 1d), significantly lower than that of NTC-4 hours, 2.54×10^{-9} S cm^{-1}. This low electronic conductivity also suggests that the measured overall conductivity using EIS is primarily due to Na-ion conduction with negligible electronic contribution.[49,50] Other Na_2O-NTC samples, regardless of different reaction times, also show low electronic conductivities on the order of 10^{-9} S cm^{-1}–10^{-10} S cm^{-1} (Fig. S3b and Table S1). Notably, Table S2 demonstrates that our Na_2O-NTC sample achieves one of the highest ionic conductivities (4.41 mS cm^{-1}) alongside a comparably low activation energy (0.32 eV), obtained *via* a short milling time of 4 hours without any thermal treatment. This performance not only matches or surpasses that of many reported sodium solid electrolytes, some of which require prolonged milling durations or additional heat treatment, but also highlights the efficiency and practicality of our synthesis approach for high-performance Na-based solid electrolytes.

Structure

The Raman spectra in Fig. 2a reveals the bonding characteristics in NTC and Na_2O–NTC. The bands at 100–200 cm^{-1} and 300–420 cm^{-1} correspond to the T_{2g} bending vibration and the A_{1g} stretching vibration of Ta–Cl, respectively.[21,35,51] In particular, the bands between 100–200 cm^{-1} originate from Ta–Cl bending modes; specifically, those below 150 cm^{-1} arise from out-of-plane bending due to Cl wagging or twisting, and those between 150–200 cm^{-1} from in-plane Cl–Ta–Cl bending. The peaks between 200–400 cm^{-1} are attributed to Ta–Cl stretching, including the intense sharp peak at ~405 cm^{-1} from axial Ta–Cl symmetric stretch and the weaker peaks at slightly lower wavenumbers from equatorial Ta–Cl symmetric stretch. The broadness of these bands in NTC and Na_2O-NTC is typical of extended 3D lattices with long-range interactions, lattice vibrations, and possible site disorder. The peak intensity decrease at ~405 cm^{-1} from axial Ta–Cl symmetric stretch suggests that O substitution of Cl mainly occurs at axial positions. Additionally, the Na_2O-NTC spectra display extra peaks between 700–900 cm^{-1}, which correspond to Ta–O–Ta stretching vibrations.[35,52] This confirms that Cl is being partially substituted by O in some of the $[TaCl_6]^-$ octahedra, with possible structural geometries illustrated in Fig. 2b.

$NaTaCl_6$ (NTC) crystallizes in the monoclinic crystal system with the space group $P2_1/n$ (ICSD #36519).[53] In its structure (Fig. 3a and b), Na, Cl, and Ta occupy the 4e Wyckoff positions. Specifically, Na^+ occupies the prismatic sites, while Ta occupies the octahedral sites; both are coordinated with chlorine ions (Fig. 3a and b). The powder XRD patterns (Fig. 3c) of Na_2O-NTC reveal a gradual disappearance of the NTC diffraction peaks with increasing ball-milling time. With 4 hours of ball-milling, Na_2O-NTC became glassy, with no significant NTC peaks remaining, leaving only a trace of NaCl impurities, as confirmed with the Rietveld refinement (Fig. 3d). This transition from a crystalline to an amorphous phase is attributed to significant structural modification of the NTC framework induced by Na_2O.

The SEM of Na_2O-NTC reveals smooth surfaces with no observable granular structures, typical of glassy materials.[35,41] This corresponds well with EIS measurements in which no grain boundary contribution to ion conduction was observed, even at low temperatures. Furthermore, the EDS mapping indicated that all the elements – Na, Ta, O, and Cl—are evenly distributed (Fig. S4). This glassy surface morphology, coupled with nearly even elemental distribution, aligns with the findings from the P-XRD analysis, reinforcing the characterization of the Na_2O-NTC as amorphous.
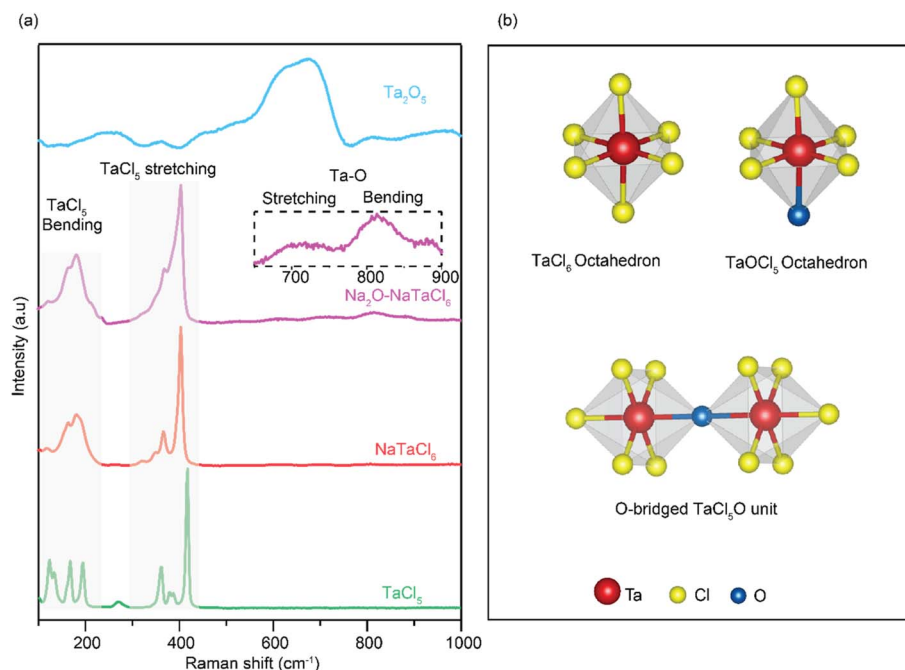

Fig. 2 (a) Raman spectra of Na_2O–$NaTaCl_6$, $NaTaCl_6$, $TaCl_5$, and Ta_2O_5. (b) Possible Ta coordinations and local geometries in Na_2O–$NaTaCl_6$.

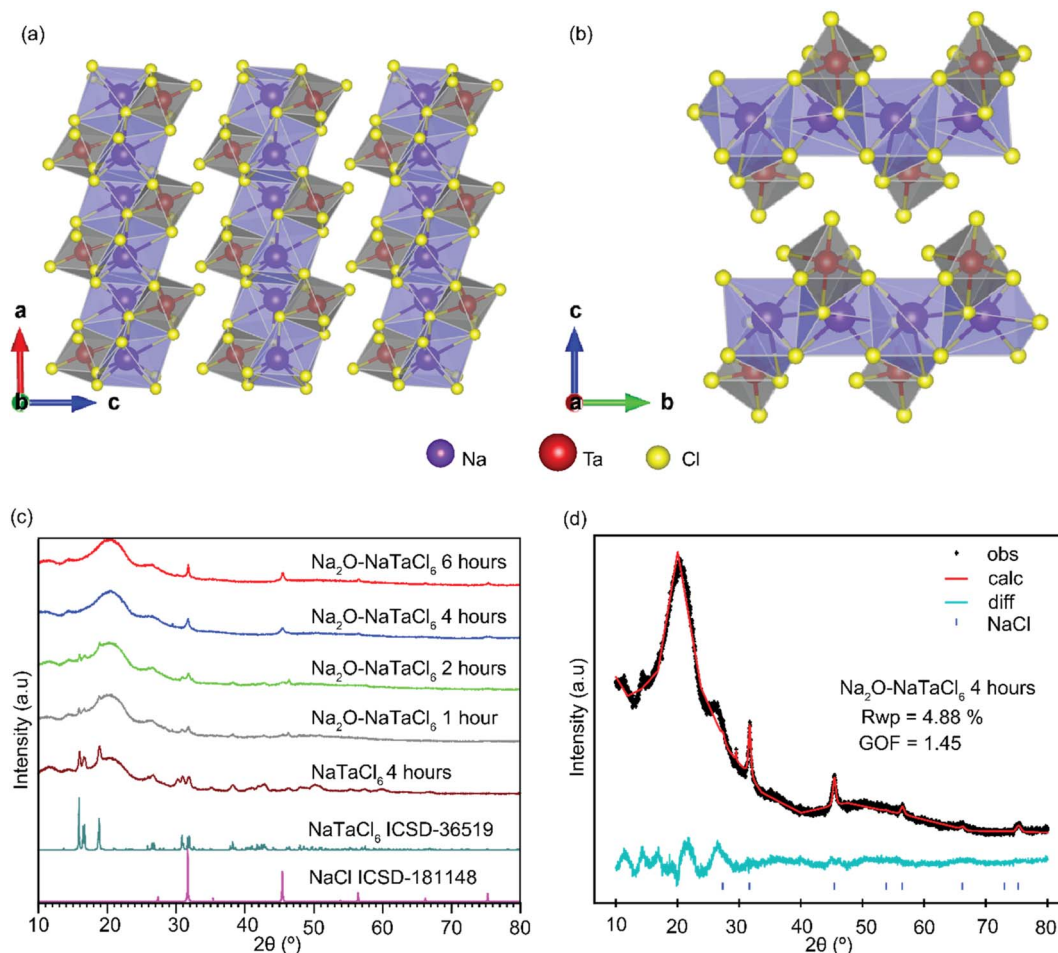Fig. 3 Crystal structure of $NaTaCl_6$ (ICSD #36519) showing Na in the prismatic site and Ta in the octahedral site, symmetry along (a) 010 and (b) 100. (c) Lab powder XRD pattern of Na_2O-$NaTaCl_6$ mechanochemically ball-milled for 1, 2, 4, and 6 hours, and $NaTaCl_6$ for 4 hours. The Broad peak at $\sim 2\theta = 20°$ originates from the Kapton film used to seal the sample container. (d) Rietveld refinement of Na_2O−$NaTaCl_6$ ball-milled for 4 hours, revealing the only crystalline phase as NaCl.

To investigate the impact of post-annealing, the most conductive Na_2O-NTC-4 hours powder was subjected to heat treatment at 150 °C for 2 hours. The corresponding EIS Nyquist plot is represented in Fig. S5. This resulted in a significant reduction in ionic conductivity, nearly two orders of magnitude lower than the as-prepared ball-milled Na_2O-NTC-4 hours (Table S3). A visible color change from creamy yellow to white was also observed after annealing, and XRD analysis revealed the gradual appearance of NTC crystalline peaks (Fig. S6). The yellow color is often attributed to a mixed-ligand Ta–O–Cl environment with an amorphous structure. The color change may be induced by crystallization and possible O loss. To further investigate the thermal stability of the as-prepared Na_2O–$NaTaCl_6$ solid electrolyte, ionic conductivity measurements were performed at progressively elevated temperatures: 25 °C, 50 °C, 75 °C, 100 °C, 150 °C, and 200 °C. As shown in Fig. S7, the conductivity decreased significantly with increasing temperature, dropping from ~ 4.41 mS cm^{-1} at 25 °C to 0.023 mS cm^{-1} at 200 °C, over two orders of magnitude lower than that of the as-prepared ball-milled Na_2O-NTC-4 hours.

Corresponding EIS Nyquist plots are provided in Fig. S7b. This significant decrease in conductivity upon heating supports the conclusion that the as-prepared material is only highly conductive in the amorphous phase. Exposure to elevated temperatures likely induces structural rearrangement or partial crystallization, which impedes Na$^+$-ion transport. These findings confirm that post-synthesis annealing is detrimental to ionic conductivity.

To evaluate the chemical stability of the solid electrolyte, an ionic-conductivity-retention test was conducted over a period of 10 days. The initial conductivity was 4.35 mS cm^{-1} and gradually decreased to 2.48 mS cm^{-1} by Day 10. Although a reduction in conductivity was observed, the electrolyte retained approximately 57% of its initial conductivity, remaining above 2 mS cm^{-1} throughout the test period (Fig. S8).

Due to the largely amorphous nature of Na_2O-NTC, Na$^+$-ion conduction is likely governed by local structural order; therefore, it is critical to acquire insights into the local structural arrangements. ^{23}Na MAS NMR experiments were utilized to probe the local structures and dynamics of Na$^+$ ions. Fig. 4
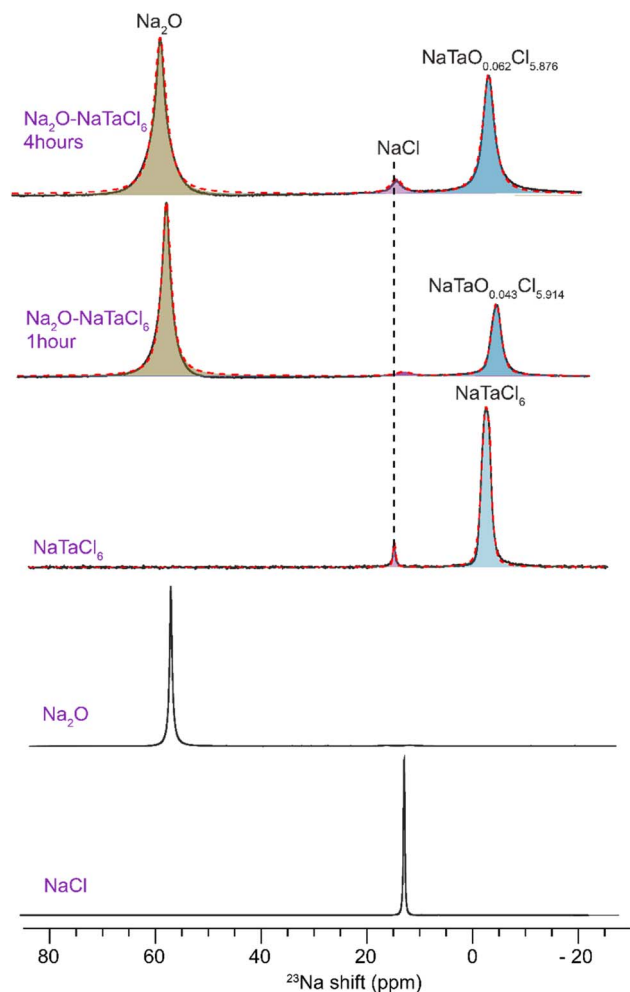
Fig. 4 ^{23}Na MAS NMR spectra of the $Na_2O-NaTaCl_6$ samples ball-milled for 4 hours and 1 hour, $NaTaCl_6$, and bulk Na_2O and NaCl.

shows the ^{23}Na MAS NMR spectra of ball-milled Na$_2$O-NTC (1 hour and 4 hours), NTC-4 hours, and bulk Na$_2$O and NaCl references. In the ^{23}Na MAS NMR spectra, crystalline NaTaCl$_6$ shows a sharp resonance at -10.6 ppm, assigned to Na$^+$ in a TaCl$_6$ octahedral environment, consistent with prior studies.[21] In contrast, the 1-h and 4-h ball-milled Na$_2$O–NaTaCl$_6$ samples exhibit similar peaks shifted upfield to -11.16 and -11.18 ppm, respectively. This shift is attributed to the formation of a disordered Na–Ta–O–Cl (NTOC) environment, supported by the Raman characterization (Fig. 2). The broader resonance and higher oxygen content in the 4-h ball-milled sample support an amorphous, oxygen-incorporated phase associated with enhanced ionic conductivity. The resonance at ∼7 ppm in all the spectra is assigned to NaCl, while the peak at ∼55 ppm in Na$_2$O-NTC samples is from Na$_2$O.[17,54] Compared with the reference spectra acquired on bulk NaCl and Na$_2$O, the NaCl and Na$_2$O resonances in Na$_2$O-NTC are significantly broader with a Lorentzian line shape; the former is indicative of structural disorder in nano-sized particles, and the latter enhanced Na$^+$-ion dynamics. In the Na$_2$O-NTC samples, the peak near ∼11 ppm broadens with increasing ball-milling time, with the linewidth increased from 274.99 Hz in NTC to 310.34 Hz (1

hour) and 380.15 Hz (4 hours) for Na$_2$O-NTC (Table S4), indicative of increased structural disorder induced by the incorporation of O, which often promotes the formation of an amorphous or glassy phase.[4] Meanwhile, the ^{23}Na MAS NMR resonance transitions from a Gaussian-dominated line shape in the NTC-4 to a Lorentzian line shape in the Na$_2$O-NTC-4 sample, suggesting ion motion-induced fast spin relaxation in the latter.

Quantitative analysis reveals a correlation between higher O-content and faster Na$^+$ dynamics in NTOC samples (Fig. S9 and Table S5). The analysis confirms that oxygen substitution within the [TaCl$_6$]$^-$ framework plays a critical role in enhancing ionic conductivity, consistent with recent MD simulations suggesting that O-for-Cl substitution in halide frameworks (NaAlCl$_{2.5}$O$_{0.75}$ and LiAlCl$_{2.5}$O$_{0.75}$) can significantly enhance Na$^+$ and Li$^+$ ionic conductivity by widening diffusion pathways and reducing migration barriers.[55]

Furthermore, the Na$_2$O-NTC-4 sample shows a higher proportion, a 30.46% increase, of the fast-conducting NaTaO$_x$-Cl$_{6-2x}$ (NTOC) phases compared to Na$_2$O-NTC-1 based on the relative integral. In the NaTaCl$_6$ sample, NaCl accounts for 5.07%, a residual from incomplete reaction of NaCl with TaCl$_5$. While in Na$_2$O-NTC samples, NaCl is a byproduct from O-incorporation into NaTaCl$_6$ (Reaction 1). NaCl amount increase from 2.29% (1 h milling) to 4.80% (4 h milling), suggesting more oxygen incorporation in the latter, which correlates with enhanced Na$^+$ mobility. The chemical compositions of NTOC in the 1-hour and 4-hour Na$_2$O-NTC NMR spectra were determined to be NaTaO$_{0.04}$Cl$_{5.92}$ and NaTaO$_{0.06}$Cl$_{5.88}$, respectively, using Chemical Reaction (1) and eqn (1) below.

$$x\,Na_2O + NaTaCl_6 \rightarrow NaTaO_xCl_{6-2x} + 2x\,NaCl \quad \text{(Reaction 1)}$$

To calculate the mole ratio of Na in the highest conductive Na$_2$O-NTC, eqn (2) was adopted:

$$2x = \frac{(\text{Area}_{\text{NaCl}})/N_{\text{NaCl}}}{(\text{Area}_{\text{NTOC}})/N_{\text{NTOC}}} \quad (1)$$

$$\frac{\text{mol A}}{\text{mol B}} = \frac{\text{Area (A)}/N\,(A)}{\text{Area (B)}/N\,(B)} \quad (2)$$

A and B represent NaCl and NTOC, respectively, and N is the number of Na per formular. Area is the areal integral of the corresponding NMR peak. The mole ratio of NTOC to NaCl was calculated to be 8 : 1.

To elucidate the role of Na$_2$O in Na$_2$O–NaTaCl$_6$ and the reaction pathways, we synthesized a comparative binary composition comprising only Na$_2$O and TaCl$_5$ in a 1 : 1 molar ratio. The reaction was carried out under similar high-energy ball milling conditions (4 hours) as used for Na$_2$O–NaCl–TaCl$_5$ (1 : 1 : 1). The Na$_2$O–TaCl$_5$ sample exhibited an ionic conductivity of 1.54 mS cm^{-1} at room temperature, whereas Na$_2$O–NaTaCl$_6$ showed a substantially higher conductivity of 4.41 mS cm^{-1} (Fig. S10a). To investigate the origin of this disparity, XRD and NMR analyses were performed on both
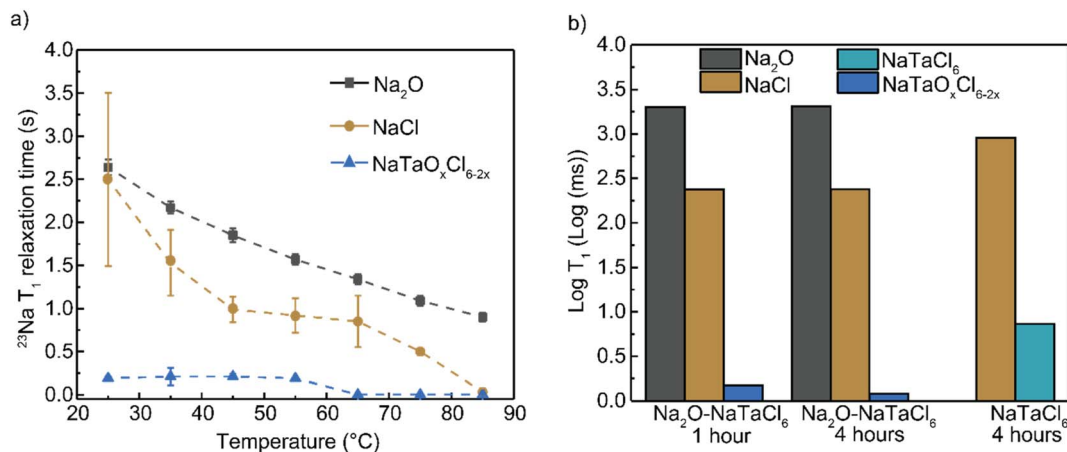
Fig. 5 (a) Variable-temperature ^{23}Na T_1 NMR relaxation times of $Na_2O-NaTaCl_6$ as a function of temperature. (b) Comparison of ^{23}Na NMR T_1 relaxation times of different components in $NaTaCl_6$ and $Na_2O-NaTaCl_6$.

samples. The $Na_2O-TaCl_5$ sample exhibits peaks corresponding to the crystalline phase of $NaTaCl_6$. In contrast, the XRD pattern of $Na_2O-NaTaCl_6$ exhibits no observable $NaTaCl_6$ peaks, confirming the formation of a fully amorphous phase (Fig. S10b). These results suggest crystalline $NaTaCl_6$ is a reaction intermediate. NMR data reveal a smaller fraction of the conductive NTOC phase with a lower O-content in the $Na_2O-TaCl_5$ sample, compared with $Na_2O-NaCl-TaCl_5$ (Fig. S9, S11 and Table S6), echoing the observed relatively lower ionic conductivity.

Na$^+$-ion dynamics

To explore the Na-ion dynamics in Na_2O-NTC, we conducted ^{23}Na T_1 NMR relaxation time measurements. The T_1 values for the NTOC, Na_2O, and NaCl resonances, measured at room temperature, were 0.0012, 2.06, and 0.24 seconds, respectively (Table S5). Notably, NTOC exhibited the shortest ^{23}Na T_1 NMR relaxation time. Significant changes in the ^{23}Na T_1 NMR relaxation times of Na_2O and NaCl before and after ball-milling are observed. The bulk forms of Na_2O and NaCl have T_1 values of 5.69 and 11.43 seconds, respectively. After ball-milling, the T_1 relaxation times decreased to 0.58 and 6.49 s for nano-sized Na_2O and NaCl. This significant drop in T_1 suggests fast spin relaxation, likely due to structural defects and distortion-enhanced quadrupolar interactions coupled with increased ion dynamics. This observation echoes with the peak broadening and Lorentzian line shape of both compounds before and after ball-milling (Fig. S12), indicating reduced crystallinity, increased structural distortions, and enhanced ion dynamics within the materials.

To further understand the relationship between ^{23}Na T_1 relaxation time and ion mobility, variable-temperature NMR (VT-NMR) was employed. According to the Bloembergen, Purcell, and Pound (BPP) theory (eqn (3)), the T_1 relaxation time relates to the motional correlation time (τ_c).[56,57] It is important to note that, in ^{23}Na (spin-3/2) NMR, quadrupolar coupling is often the dominant interaction in asymmetric local environments, which, when coupled with ion dynamics at a rate in the vicinity of the ^{23}Na Larmor frequency, drives fast spin relaxation

(eqn (3)). Fast spin relaxation often yields a typical Lorentzian line shape, as we observed in Fig. 4.

$$\frac{1}{T_1} = \frac{3}{200}Q_c\left(1 + \frac{\eta^2}{3}\right) \times \frac{2I+3}{I^2(2I-1)}\left[\frac{\tau_c}{1+\omega_0^2\tau_c^2} + \frac{4\tau_c}{1+4\omega_0^2\tau_c^2}\right]$$

(3)

where T_1 is the spin-lattice relaxation time, I is the nuclei spin number (3/2 for ^{23}Na), Q_c is the nuclear quadrupolar coupling constant, η is the asymmetry parameter, ω_0 is the Larmor frequency, and τ_c is the motional correlation time constant. Fig. 5 demonstrates that as the temperature increases, the ^{23}Na T_1 values decrease for all resonances, indicating that all resonances are in the slow-motion regime ($w_0\ \tau_c >> 1$) and that shorter T_1 values correlate to faster Na-ion mobility. Therefore, NTOC exhibits fastest Na$^+$ dynamics in Na_2O-NTC, because of the shortest T_1 relaxation time of 1.2 ms among the Na-containing species in Na_2O-NTC. In comparison, the ^{23}Na T_1 for Na in NTC is 7.3 ms, longer than that for NTOC, suggesting slower Na$^+$ dynamics. The other components, Na_2O and NaCl, show much longer ^{23}Na T_1 values and limited ion exchange with NTC or NTOC, likely no significant contribution to overall ionic conductivity. Additionally, the electrochemical impedance measurements of ball-milled NaCl and Na_2O exhibited very large impedance. The Nyquist plots appear scattered and do not form a semicircle because Na_2O and NaCl are poor ion conductors with very high resistance. Consequently, the impedance response is dominated by noise and measurement limitations, preventing the formation of a clear semicircle typically seen in ionically conductive materials (Fig. S13).

Conclusion

In this study, we report a glassy sodium solid electrolyte $Na_2O-NaTaCl_6$. Using a one-step room-temperature mechanochemical synthesis over 4 hours, we achieved a high ionic conductivity of 4.41 mS cm^{-1} and an activation energy of 0.32 eV. P-XRD on $Na_2O-NaTaCl_6$ revealed a highly disordered structure. The SEM-EDS analysis showed no significant grain boundaries and a homogenous distribution of Na, Ta, O, and Cl. The

Raman analysis confirmed the substitution of Cl with O to form NTOC. High-resolution ^{23}Na NMR spectroscopy quantifies the amount of O incorporated into NTOC and NMR relaxometry revealed fast Na$^+$-ion dynamics in NTOC, which is responsible for the observed fast Na-ion conduction. Na$_2$O acted as a glass modifier that facilitated the formation of the highly conductive glassy phase within a short time of mechanochemical synthesis, compared with typical duration of tens of hours. This study underscores the role of glass modifiers in creating superionic conductors with strong potential for cost-effective, commercially viable solid electrolytes.

Author contributions

Islamiyat A. Ojelade: data curation: lead; investigation: supporting; validation: supporting; vsualization: lead; writing – original draft: lead. Erica Truong: data curation: lead; investigation: supporting; validation: supporting; visualization: lead; writing – original draft: lead. Ifeoluwa P. Oyekunle: data curation: supporting; formal analysis: supporting; investigation: supporting; methodology: supporting; validation: supporting; visualization: supporting; writing – original draft: supporting. Tej P. Poudel: data curation: supporting; formal analysis: supporting; investigation: supporting; methodology: supporting; validation: supporting; visualization: supporting; writing – original draft: supporting. Yudan Chen: data curation: supporting; formal analysis: supporting; investigation: supporting; methodology: supporting; software: supporting; writing – origwnal draft: supporting. Michael J. Deck: data curation: supporting investigation: supporting; validation: supporting; visualization: supporting; writing – original draft: supporting. Yongkang Jin: data curation: supporting investigation: supporting; validation: supporting; writing – original draft: supporting. Bright Ogbolu: investigation: supporting; validation: supporting; visualization: supporting; writing – review & editing: supporting. Md. Mahinur Islam: data curation: supporting; validation: supporting; writing – review & editing: supporting. Pawan K. Ojha: data curation: supporting; validation: supporting; writing – review & editing: supporting. Thilina N. D. D. Gamaralalage: validation: supporting; visualization: supporting; writing – review & editing: supporting. J. S. Raaj Vellore Winfred: data curation: supporting; formal analysis: supporting. Yan-Yan Hu, Ph.D.: conceptualization: lead; formal analysis: lead; funding acquisition: lead; methodology: lead; project administration: lead; resources: lead; supervision: lead; validation: lead; visualization: equal; writing – original draft: equal; writing – review & editing: lead.

Conflicts of interest

The authors declare no conflict of interest.

Data availability

The data supporting this article have been included as part of the SI. Supplementary information is available. See DOI: https://doi.org/10.1039/d5sc05307b.

References

1 H. Ahmad, K. T. Kubra, A. Butt, U. Nisar, F. J. Iftikhar and G. Ali, Recent Progress, Challenges, and Perspectives in the Development of Solid-State Electrolytes for Sodium Batteries, *J. Power Sources*, 2023, **581**, 233518, DOI: **10.1016/j.jpowsour.2023.233518**.

2 L. Fan, S. Wei, S. Li, Q. Li and Y. Lu, Recent Progress of the Solid-State Electrolytes for High-Energy Metal-Based Batteries, *Adv. Energy Mater.*, 2018, **8**(11), 1702657, DOI: **10.1002/aenm.201702657**.

3 J. Kim, K. Yoon, I. Park and K. Kang, Progress in the Development of Sodium-Ion Solid Electrolytes, *Small Methods*, 2017, **1**(10), 1700219, DOI: **10.1002/smtd.201700219**.

4 M. J. Deck, Po-H. Chien, T. P. Poudel, Y. Jin, H. Liu and Y.-Y. Hu, Oxygen-Induced Structural Disruption for Improved Li$^+$ Transport and Electrochemical Stability of Li$_3$PS$_4$, *Adv. Energy Mater.*, 2024, **14**(4), 2302785, DOI: **10.1002/aenm.202302785**.

5 K. H. Park, Q. Bai, D. H. Kim, D. Y. Oh, Y. Zhu, Y. Mo and Y. S. Jung, Design Strategies, Practical Considerations, and New Solution Processes of Sulfide Solid Electrolytes for All-Solid-State Batteries, *Adv. Energy Mater.*, 2018, **8**(18), 1800035, DOI: **10.1002/aenm.201800035**.

6 J. C. Bachman, S. Muy, A. Grimaud, H.-H. Chang, N. Pour, S. F. Lux, O. Paschos, F. Maglia, S. Lupart, P. Lamp, L. Giordano and Y. Shao-Horn, Inorganic Solid-State Electrolytes for Lithium Batteries: Mechanisms and Properties Governing Ion Conduction, *Chem. Rev.*, 2016, **116**(1), 140–162, DOI: **10.1021/acs.chemrev.5b00563**.

7 T. Poudel, M. J. Deck, P. Wang and Y.-Y. Hu, Transforming Li$_3$PS$_4$ Via Halide Incorporation: A Path to Improved Ionic Conductivity and Stability in All-Solid-State Batteries, *Adv. Funct. Mater.*, 2024, **34**(4), 2309656, DOI: **10.1002/adfm.202309656**.

8 Y. Lian, M. Wu, B. Xu, B. He, G. Liu, J. Shi, Q. Kuang, H. Wang and C. Ouyang, Phase-Structure Design for Sodium Chloride Solid Electrolytes with Outstanding Performance: A First-Principles Approach, *J. Mater. Chem. A*, 2023, **11**(4), 1906–1919, DOI: **10.1039/D2TA07603A**.

9 G. Liu, J. Yang, J. Wu, Z. Peng and X. Yao, Inorganic Sodium Solid Electrolytes: Structure Design, Interface Engineering and Application, *Adv. Mater.*, 2024, 2311475, DOI: **10.1002/adma.202311475**.

10 Z. Li, P. Liu, K. Zhu, Z. Zhang, Y. Si, Y. Wang and L. Jiao, Solid-State Electrolytes for Sodium Metal Batteries, *Energy*

Fuels, 2021, **35**(11), 9063–9079, DOI: **10.1021/acs.energyfuels.1c00347**.

11 Q. Zhao, S. Stalin, C.-Z. Zhao and L. A. Archer, Designing Solid-State Electrolytes for Safe, Energy-Dense Batteries, *Nat. Rev. Mater.*, 2020, **5**(3), 229–252, DOI: **10.1038/s41578-019-0165-5**.

12 M. Hou, F. Liang, K. Chen, Y. Dai and D. Xue, Challenges and Perspectives of NASICON-Type Solid Electrolytes for All-Solid-State Lithium Batteries, *Nanotechnology*, 2020, **31**(13), 132003, DOI: **10.1088/1361-6528/ab5be7**.

13 J. B. Goodenough, H. Y.-P. Hong and J. A. Kafalas, Fast Na+-Ion Transport in Skeleton Structures, *Mater. Res. Bull.*, 1976, **11**(2), 203–220, DOI: **10.1016/0025-5408(76)90077-5**.

14 S. R. Keshri, S. Ganisetti, R. Kumar, A. Gaddam, K. Illath, T. G. Ajithkumar, S. Balaji, K. Annapurna, N. Nasani, N. M. A. Krishnan and A. R. Allu, Ionic Conductivity of $Na_3Al_2P_3O_{12}$ Glass Electrolytes—Role of Charge Compensators, *Inorg. Chem.*, 2021, **60**(17), 12893–12905, DOI: **10.1021/acs.inorgchem.1c01280**.

15 M. Samiee, B. Radhakrishnan, Z. Rice, Z. Deng, Y. S. Meng, S. P. Ong and J. Luo, Divalent-Doped Na3Zr2Si2PO12 Natrium Superionic Conductor: Improving the Ionic Conductivity via Simultaneously Optimizing the Phase and Chemistry of the Primary and Secondary Phases, *J. Power Sources*, 2017, **347**, 229–237, DOI: **10.1016/j.jpowsour.2017.02.042**.

16 A. Hayashi, K. Noi, A. Sakuda and M. Tatsumisago, Superionic Glass-Ceramic Electrolytes for Room-Temperature Rechargeable Sodium Batteries, *Nat. Commun.*, 2012, **3**(1), 856, DOI: **10.1038/ncomms1843**.

17 Y.-Y. H. Xuyong Feng, Po-H. Chien, I.-H. Chu, P. Wang, M. Immediato-Scuotto, H. Arabzadeh and S. P. Ong, Studies of Functional Defects for Fast Na-Ion Conduction in Na3−yPS4−xClx with a Combined Experimental and Computational Approach, *Adv. Funct. Mater.*, 2019, **29**(9), 1807951, DOI: **10.1002/adfm.201807951**.

18 H. Nguyen, A. Banerjee, X. Wang, D. Tan, E. A. Wu, J.-M. Doux, R. Stephens, G. Verbist and Y. S. Meng, Single-Step Synthesis of Highly Conductive Na3PS4 Solid Electrolyte for Sodium All Solid-State Batteries, *J. Power Sources*, 2019, **435**, 126623, DOI: **10.1016/j.jpowsour.2019.05.031**.

19 S. Takeuchi, K. Suzuki, M. Hirayama and R. Kanno, Sodium Superionic Conduction in Tetragonal Na3PS4, *J. Solid State Chem.*, 2018, **265**, 353–358, DOI: **10.1016/j.jssc.2018.06.023**.

20 W. Tang, R. Qi, J. Wu, Y. Zuo, Y. Shi, R. Liu, W. Yan and J. Zhang, Engineering, Understanding, and Optimizing Electrolyte/Anode Interfaces for All-Solid-State Sodium Batteries, *Electrochem. Energy Rev.*, 2024, **7**(1), 23, DOI: **10.1007/s41918-024-00228-7**.

21 X. Sun, Hu Yang, J. Fu, J. Xu and J. Luo, Superionic Amorphous NaTaCl6 Halide Electrolyte for Highly Reversible All-Solid-State Na-Ion Batteries, *Mater*, 2024, **7**(3), 1018–1034, DOI: **10.1016/j.matt.2023.12.017**.

22 R. Li, K. Xu, S. Wen, X. Tang, Z. Lin, X. Guo, M. Avdeev, Z. Zhang and Y. Hu, A sodium superionic chloride electrolyte driven by paddle wheel mechanism for solid

state batteries, *Nat. Commun.*, 2025, **16**(6633), 1–18, DOI: **10.1038/s41467-025-61738-6**.

23 K. Motohashi, H. Tsukasaki, A. Sakuda, S. Mori and A. Hayashi, $NaTaCl_6$: Chloride as the End-Member of Sodium-Ion Conductors, *ACS Mater. Lett.*, 2024, **6**(4), 1178–1183, DOI: **10.1021/acsmaterialslett.3c01445**.

24 R. Schlem, A. Banik, M. Eckardt, M. Zobel and W. G. Zeier, Na$_{3−x}$Er$_{1−x}$Zr$_x$Cl$_6$—A Halide-Based Fast Sodium-Ion Conductor with Vacancy-Driven Ionic Transport, *ACS Appl. Energy Mater.*, 2020, **3**(10), 10164–10173, DOI: **10.1021/acsaem.0c01870**.

25 H. Kwak, J. Lyoo, J. Park, Y. Han, R. Asakura, A. Remhof, C. Battaglia, H. Kim, S.-T. Hong and Y. S. Jung, Na2ZrCl6 Enabling Highly Stable 3 V All-Solid-State Na-Ion Batteries, *Energy Storage Mater.*, 2021, **37**, 47–54, DOI: **10.1016/j.ensm.2021.01.026**.

26 E. A. Wu, S. Banerjee, H. Tang, P. M. Richardson, J.-M. Doux, J. Qi, Z. Zhu, A. Grenier, Y. Li, E. Zhao, G. Deysher, E. Sebti, H. Nguyen, R. Stephens, G. Verbist, K. W. Chapman, R. J. Clément, A. Banerjee, Y. S. Meng and S. P. Ong, A Stable Cathode-Solid Electrolyte Composite for High-Voltage, Long-Cycle-Life Solid-State Sodium-Ion Batteries, *Nat. Commun.*, 2021, **12**(1), 1256, DOI: **10.1038/s41467-021-21488-7**.

27 J. Park, J. P. Son, W. Ko, J.-S. Kim, Y. Choi, H. Kim, H. Kwak, D.-H. Seo, J. Kim and Y. S. Jung, $NaAlCl_4$: New Halide Solid Electrolyte for 3 V Stable Cost-Effective All-Solid-State Na-Ion Batteries, *ACS Energy Lett.*, 2022, **7**(10), 3293–3301, DOI: **10.1021/acsenergylett.2c01514**.

28 Z. Huang, S. Yoshida, H. Akamatsu, K. Hayashi and S. Ohno, NaMCl$_6$ (M = Nb and Ta): A New Class of Sodium-Conducting Halide-Based Solid Electrolytes, *ACS Mater. Lett.*, 2024, **6**(5), 1732–1738, DOI: **10.1021/acsmaterialslett.4c00315**.

29 H. Yang and N. Wu, Ionic Conductivity and Ion Transport Mechanismsof Solid-state Lithium-ion Battery Electrolytes: A Review, *Energy Sci. Eng.*, 2022, **10**(5), 1643–1671, DOI: **10.1002/ese3.1163**.

30 J. Wolfenstine, J. L. Allen, J. Sakamoto, D. J. Siegel and H. Choe, Mechanical Behavior of Li-Ion-Conducting Crystalline Oxide-Based Solid Electrolytes: A Brief Review, *Ionics*, 2018, **24**(5), 1271–1276, DOI: **10.1007/s11581-017-2314-4**.

31 W. Zhixuan, F. N. Linda and J. Jürgen, Emerging Halide Solid Electrolytes for Sodium Solid-State Batteries: Structure, Conductivity, Paradigm of Applications, *Batteries Supercaps*, 2024, **7**(7), e202400005, DOI: **10.1002/batt.202400005**.

32 H. Liu, Y. Chen, Po-H. Chien, G. Amouzandeh, D. Hou, E. Truong, I. P. Oyekunle, J. Bhagu, S. W. Holder, H. Xiong, P. L. Gor'kov, J. T. Rosenberg, S. C. Grant and Y.-Y. Hu, Dendrite Formation in Solid-State Batteries Arising from Lithium Plating and Electrolyte Reduction, *Nat. Mater.*, 2025, **24**, 581–588, DOI: **10.1038/s41563-024-02094-6**.

33 J. L. Souquet, Ionic Transport in Amorphous Solid Electrolytes, *Annu. Rev. Mater. Sci.*, 1981, **11**(1), 211–231, DOI: **10.1146/annurev.ms.11.080181.001235**.

34 Y. Fujita, T. Kimura, M. Deguchi, K. Motohashi, A. Sakuda, M. Tatsumisago, H. Tsukasaki, S. Mori, K. Ikeda, K. Ohara,

N. Kuwata, K. Amezawa and A. Hayashi, Structural Investigation of Li 2 O–LiI Amorphous Solid Electrolytes, *J. Phys. Chem. C*, 2023, **127**(30), 14687–14693, DOI: **10.1021/acs.jpcc.3c03876**.

35 S. Zhang, F. Zhao, J. Chen, J. Fu, J. Luo, S. H. Alahakoon, L.-Y. Chang, R. Feng, M. Shakouri, J. Liang, Y. Zhao, X. Li, L. He, Y. Huang, T.-K. Sham and X. Sun, A Family of Oxychloride Amorphous Solid Electrolytes for Long-Cycling All-Solid-State Lithium Batteries, *Nat. Commun.*, 2023, **14**(1), 3780, DOI: **10.1038/s41467-023-39197-8**.

36 A. Levasseur, J.-C. Brethous, M. Kbala and P. Hagenmuller, Synthesis and Characterization of New Amorphous Solid Electrolytes, *Solid State Ionics*, 1981, **5**, 651–654, DOI: **10.1016/0167-2738(81)90338-6**.

37 D. Ravaine, Glasses as Solid Electrolytes, *J. Non-Cryst. Solids*, 1980, **38–39**, 353–358, DOI: **10.1016/0022-3093(80)90444-5**.

38 H. W. Nesbitt, G. M. Bancroft, G. S. Henderson, R. Ho, K. N. Dalby, Y. Huang and Z. B. Yan, Non-Bridging and Free (O2−) Oxygen in Na2O-SiO2 Glasses: An X-Ray Photoelectron Spectroscopic (XPS) and Nuclear Magnetic Resonance (NMR) Study, *J. Non-Cryst. Solids*, 2011, **357**(1), 170–180, DOI: **10.1016/j.jnoncrysol.2010.09.031**.

39 A. Karthikeyan, P. Vinatier, A. Levasseur and K. J. Rao, The Molecular Dynamics Study of Lithium Ion Conduction in Phosphate Glasses and the Role of Non-Bridging Oxygen, *J. Phys. Chem. B*, 1999, **103**(30), 6185–6192, DOI: **10.1021/jp990228c**.

40 G. Jayasinghe, Electrical Properties of TeO2 Glasses with Na2O as Network Modifier, *Solid State Ionics*, 1995, **76**(3–4), 297–300, DOI: **10.1016/0167-2738(94)00287-3**.

41 A. Chandra, A. Bhatt and A. Chandra, Ion Conduction in Superionic Glassy Electrolytes: An Overview, *J. Mater. Sci. Technol.*, 2013, **29**(3), 193–208, DOI: **10.1016/j.jmst.2013.01.005**.

42 M. Ribes, B. Barrau and J. L. Souquet, Sulfide glasses: Glass forming region, structure and ionic conduction of glasses in Na₂S-XS₂ (X-Si; Ge), Na₂S-P₂S₅ and Li₂S-GeS₂ systems, *J. Non-Cryst. Solids*, 1980, **38**(1), 271–276, DOI: **10.1016/0022-3093(80)90430-5**.

43 K. Noi, A. Hayashi and M. Tatsumisago, Structure and Properties of the Na2S–P2S5 Glasses and Glass–Ceramics Prepared by Mechanical Milling, *J. Power Sources*, 2014, **269**, 260–265, DOI: **10.1016/j.jpowsour.2014.06.158**.

44 S. Zhao, H. Che, S. Chen, H. Tao, J. Liao, X.-Z. Liao and Z.-F. Ma, Research Progress on the Solid Electrolyte of Solid-State Sodium-Ion Batteries, *Electrochem. Energy Rev.*, 2024, 7(1), 3, DOI: **10.1007/s41918-023-00196-4**.

45 B. H. Toby, EXPGUI , a Graphical User Interface for GSAS, *J. Appl. Crystallogr.*, 2001, **34**(2), 210–213, DOI: **10.1107/S0021889801002242**.

46 M. Uitz, V. Epp, P. Bottke and M. Wilkening, Ion Dynamics in Solid Electrolytes for Lithium Batteries: Probing Jump Rates and Activation Energies through Time-Domain Li NMR, *J. Electroceram.*, 2017, **38**(2–4), 142–156, DOI: **10.1007/s10832-017-0071-4**.

47 A. Ch. Lazanas and M. I. Prodromidis, Electrochemical Impedance Spectroscopy–A Tutorial, *ACS Meas. Sci. Au*, 2023, **3**(3), 162–193, DOI: **10.1021/acsmeasuresciau.2c00070**.

48 B.-A. Mei, O. Munteshari, J. Lau, B. Dunn and L. Pilon, Physical Interpretations of Nyquist Plots for EDLC Electrodes and Devices, *J. Phys. Chem. C*, 2018, **122**(1), 194–206, DOI: **10.1021/acs.jpcc.7b10582**.

49 L. Zhou, T.-T. Zuo, C. Y. Kwok, S. Y. Kim, A. Assoud, Q. Zhang, J. Janek and L. F. Nazar, High Areal Capacity, Long Cycle Life 4 V Ceramic All-Solid-State Li-Ion Batteries Enabled by Chloride Solid Electrolytes, *Nat. Energy*, 2022, **7**(1), 83–93, DOI: **10.1038/s41560-021-00952-0**.

50 I. Kochetkov, T.-T. Zuo, R. Ruess, B. Singh, L. Zhou, K. Kaup, J. Janek and L. Nazar, Different Interfacial Reactivity of Lithium Metal Chloride Electrolytes with High Voltage Cathodes Determines Solid-State Battery Performance, *Energy Environ. Sci.*, 2022, **15**(9), 3933–3944, DOI: **10.1039/D2EE00803C**.

51 L. C. Gerald, Vibrational Spectra of Some MC!& Molecules : SbCl, PCl, TaCl, and NbCl, *Spectrochimica Acta*, 1963, **19**, 1219–1307, DOI: **10.1016/0371-1951(63)80239-8**.

52 O. B. Babushkina, S. Ekres and G. E. Nauer, Spectroscopy and Electrochemistry of Tantalum(V) in 1-Butyl-1-Methylpyrrolidinium Trifluoromethanesulfonate, *Z. Naturforsch. A*, 2008, **63**(1–2), 73–80, DOI: **10.1515/zna-2008-1-213**.

53 D. Park, K. Kim, G. H. Chun, B. C. Wood, J. H. Shim and S. Yu, Materials Design of Sodium Chloride Solid Electrolytes Na 3 MCl 6 for All-Solid-State Sodium-Ion Batteries, *J. Mater. Chem. A*, 2021, **9**(40), 23037–23045, DOI: **10.1039/D1TA07050A**.

54 Z. E. M. Reeve, C. J. Franko, K. J. Harris, H. Yadegari, X. Sun and G. R. Goward, Detection of Electrochemical Reaction Products from the Sodium–Oxygen Cell with Solid-State23 Na NMR Spectroscopy, *J. Am. Chem. Soc.*, 2017, **139**(2), 595–598, DOI: **10.1021/jacs.6b11333**.

55 T. Dai, S. Wu, Y. Lu, Y. Yang, Y. Liu, C. Chang, X. Rong, R. Xiao, J. Zhao, Y. Liu, W. Wang, L. Chen and Y.-S. Hu, Inorganic Glass Electrolytes with Polymer-like Viscoelasticity, *Nat. Energy*, 2023, **8**(11), 1221–1228, DOI: **10.1038/s41560-023-01356-y**.

56 N. Bloembergen, E. M. Purcell and R. V. Pound, Relaxation Effects in Nuclear Magnetic Resonance Absorption, *Phys. Rev.*, 1948, **73**(7), 679–712, DOI: **10.1103/PhysRev.73.679**.

57 C. V. Amanchukwu, A. B. Gunnarsdóttir, S. Choudhury, T. L. Newlove, P. C. M. M. Magusin, Z. Bao and C. P. Grey, Understanding Lithium-Ion Dynamics in Single-Ion and Salt-in-Polymer Perfluoropolyethers and Polyethyleneglycol Electrolytes Using Solid-State NMR, *Macromeolecules*, 2023, **56**(10), 3650–3659.